Proper Ferroelectricity in the Dion−Jacobson Material CsBi$_2$Ti$_2$NbO$_{10}$: Experiment and Theory

Emma E. McCabe,*[,†] Eric Bousquet,[‡] Christopher P. J. Stockdale,[†] Charles A. Deacon,[†] T. Thao Tran,[§] P. Shiv Halasyamani,[§] Martin C. Stennett,[∥] and Neil C. Hyatt*[,∥]

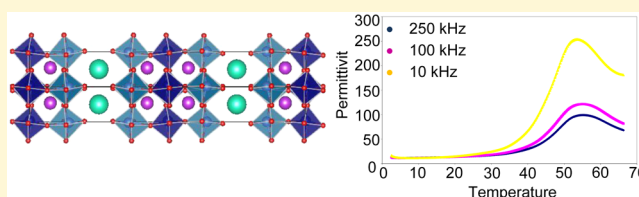[†]School of Physical Sciences, Ingram Building, University of Kent, Canterbury, Kent, CT2 7NH, U.K.

[‡]Université de Liège, Institut de Physique B5a, Allée du 6 Août, 17, B-4000 Sart Tilman, Belgium

[§]Department of Chemistry, University of Houston, 112 Fleming Building, Houston, Texas 77204-5003, United States

[∥]Department of Materials Sciences and Engineering, University of Sheffield, Sir Robert Hadfield Building, Mappin Street, Sheffield S1 3JD, U.K.

S *Supporting Information*

ABSTRACT: A diverse range of materials and properties are exhibited by layered perovskites. We report on the synthesis, characterization, and computational investigation of a new ferroelectric—CsBi$_2$Ti$_2$NbO$_{10}$—an n = 3 member of the Dion−Jacobson (DJ) family. Structural studies using variable-temperature neutron powder diffraction indicate that a combination of octahedral rotations and polar displacements result in the polar structure. Density functional theory calculations reveal that the wider perovskite blocks in CsBi$_2$Ti$_2$NbO$_0$ stabilize proper ferroelectricity, in contrast to the hybrid-improper ferroelectricity reported for all other DJ phases. Our results raise the possibility of a new class of proper ferroelectric materials analogous to the well-known Aurivillius phases.

INTRODUCTION

Ferroelectric materials, i.e., polar materials where the macroscopic polarization may be reversed or switched, are an important class of compounds due to their academic and technological relevance. From an academic perspective, the mechanisms that give rise to the polarization have fascinated chemists, physicists, and materials scientists, and understanding them has allowed the design and preparation of new classes of functional materials. Technologically, ferroelectrics are used in applications such as random-access memories,[1,2] sensors, and thin-film capacitors.[3] Structurally, all ferroelectric materials must be crystallographically polar. Layered perovskite-related materials, including the Ruddlesden−Popper (RP), Aurivillius, and Dion−Jacobson (DJ) families, not only are an important class of ferroelectric materials but also represent ideal structural families in which to explore the mechanisms that give rise to polar structures. These include second-order Jahn−Teller driven cation displacements, cation ordering patterns, and combinations of nonpolar octahedral rotations.[4]

DJ phases, of general formula $A'A_{n-1}B_nO_{3n+1}$, consist of perovskite blocks composed of n layers of corner-linked BO_6 octahedra, separated by layers of alkali A' cations. The ideal, aristotype structure is tetragonal (of $P4/mmm$ symmetry, Figure 1) with unit cell $a_t \approx 3.8$ Å$\times c_t$ ("t" denotes tetragonal unit cell in this work). Depending on the size of the A' cation, the perovskite blocks are stacked in an eclipsed conformation (for larger A' cations, e.g., Rb$^+$, Cs$^+$) or in a staggered conformation (for smaller A' cations, e.g., K$^+$, Na$^+$). The two stacking arrangements both differ from that in the RP and Aurivillius families (in which successive blocks are offset by ($^1/_2a$, $^1/_2b$) translation).

The structural chemistry of the DJ family is not yet fully understood, and although distortions similar to those found in RP and Aurivillius materials (e.g., rotation of BO_6 octahedra, cation displacements) can be expected in the DJ phases, the symmetries of the resulting DJ phase will not necessarily follow those determined for the related RP and Aurivillius phases.[5−8]

Rigorous DFT calculations by Fennie and Rabe predicted ferroelectric behavior in the n = 2 DJ phase CsBiNb$_2$O$_7$.[9] Careful structural work has shown that CsBiNb$_2$O$_7$ adopts a polar, orthorhombic structure ($P2_1am$ symmetry, $\sqrt{2}a_t \times \sqrt{2}a_t' \times c_t$) up to at least 900 °C. This polar structure is derived from the aristotype tetragonal structure by rotation of NbO$_6$ octahedra around both an in-plane axis ([110]$_t$, $a^-a^-c^0$ in Glazer notation, corresponding to the M5− rotational mode) and the tetragonal axis [001]$_t$ ($a^0a^0c^+$ in Glazer notation, corresponding to the M2+ rotational mode), and by ferroelectric displacement of Bi^{3+} cations along the polar a axis.[10,11] This is analogous to the structure of ferroelectric SrBi$_2$Ta$_2$O$_9$ (and related off-stoichiometric phases).[12,13] However, demonstration of its ferroelectric behavior has proven difficult.[10,11] Investigations using X-ray powder diffraction (XRPD) suggest

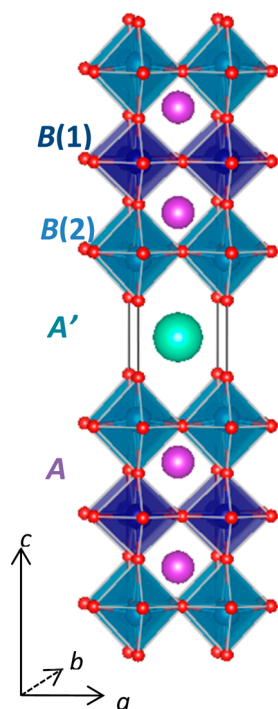**Figure 1.** Illustration of the aristotype, high-temperature structure of $CsBi_2Ti_2NbO_{10}$ described by $P4/mmm$ symmetry, showing Cs, Bi, and Ti/Nb cations in green, purple, and blue, respectively, and $B(1)O_6$ and $B(2)O_6$ octahedra in dark and pale blue.

that $RbBiNb_2O_7$ is isostructural to $CsBiNb_2O_7$, and property measurements show that this Rb analogue has a relatively low permittivity and a ferroelectric $T_C \approx 945$ °C.[14] More recently, Benedek has demonstrated the importance of "hybrid-improper" mechanisms for ferroelectricity in these $n = 2$ DJ phases. This has prompted further work[15,16] including piezoresponse force microscopy studies which have demonstrated the ferroelectric and piezoelectric behavior of $A'BiNb_2O_7$ (A' = Cs, Rb).[17]

Structural characterization of $n = 3$ DJ phases ($RbA_2M_3O_{10}$, A = Ca, Sr and M = Nb, Ta;[18] $CsLn_2Ti_2NbO_{10}$, Ln = La, Pr, Nd, Sm;[19] $A'A_2M_3O_{10}$, A' = Rb, Cs, A = Sr, Ba, and M = Nb, Ta[20]) using XRPD data has suggested the possibility of structural distortions involving octahedral tilting in the $n = 3$ series of DJ phases, but this has not been thoroughly investigated. We report here structural studies from variable-temperature neutron powder diffraction (NPD) data on the $n = 3$ DJ phase $CsBi_2Ti_2NbO_{10}$ and show that it adopts a polar structure at room temperature involving two modes of octahedral rotation as well as ferroelectric displacements along the in-plane polar direction. At ~540 °C, $CsBi_2Ti_2NbO_{10}$ undergoes a phase transition to a higher symmetry tetragonal phase. These structural studies are consistent with second harmonic generation (SHG) tests and its relatively low permittivity with maximum at ~550 °C and are discussed in the light of recent work on hybrid-improper ferroelectrics.[21,22] DFT calculations show that $CsBi_2Ti_2NbO_{10}$ is a proper ferroelectric, unlike the $n = 2$ analogues, and are used to explore structural instabilities of this system.

■ EXPERIMENTAL AND CALCULATION DETAILS

Polycrystalline samples of $CsBi_{2-x}La_xTi_2NbO_{10}$ were prepared by reacting stoichiometric quantities of Cs_2CO_3 (in 30% excess to account for volatility), Bi_2O_3, La_2O_3, TiO_2, and Nb_2O_5. These reagents

were ground by hand in an agate mortar and pestle under an acetone slurry and pressed into 10 mm diameter pellet(s). The resulting mixture was placed in an alumina boat and heated at 550 °C for 6 h, followed by 12 h at 850 °C. After cooling to room temperature in the furnace, the sample was ground under an acetone slurry and reheated at 850 °C for 12 h, and this process was repeated several times. Finally, the powder was washed several times with cold, deionized water and recovered by vacuum filtration. Preliminary characterization was carried out using XRPD using a Bruker D8 Advance diffractometer operating in reflection mode with Cu Kα source and a Vantec detector.

Neutron powder diffraction data were collected on the time-of-flight (TOF) diffractometer POLARIS at the ISIS spallation neutron source. High quality data sets were collected at 25, 200, 360, 440, 480, 500, 515, 545, and 700 °C, and shorter data collections were made at 280, 400, 460, 525, 535, 600, and 650 °C. Diffraction data were analyzed using the Rietveld method[23] using Topas Academic software.[24,25] Sequential refinements were carried out using local subroutines. Some peaks from vanadium were observed in the NPD data (presumably from the sample can), and these were fitted with a body-centered cubic vanadium phase in refinements. Distortions and group−subgroup relations were explored using the symmetry-adapted distortion mode approach, and ISODISTORT[26] was used to give symmetry mode descriptions of distorted structures for use in Rietveld refinements using Topas Academic. Preferred orientation was modeled (where described in the text) using a March−Dollase function with a single preferred orientation direction, consistent with a plate-like morphology.[27,28]

The samples were tested for SHG using the experimental setup described in ref 29. The diffuse reflectance spectra were recorded by placing sample ground with dry sodium chloride (~10% w/w) in an optical cuvette and illuminating it with a halogen lamp (Ocean Optics DH-2000-S). Nonspecular scattered light was collected, and the spectrum was recorded using an OceanOptics spectrometer (Mayer2000 Pro). A cuvette of ground sodium chloride was used as a reference. The data were used to calculate the reflectance spectra $R(I)$ and Kubelka−Munk spectra $F(R)$.[30]

Pellets of 5 mm diameter of $CsBi_2Ti_2NbO_{10}$ were heated at 2 °C min^{-1} to a sintering temperature of 850 °C and held at this temperature for 4 h. During this sintering process, the pellets were embedded in a sacrificial powder of the same composition as the sample. This gave pellets of density ~83% of their theoretical density. Gold electrodes were attached to sintered pellets of $CsBi_2Ti_2NbO_{10}$ using gold paste (annealed at 800 °C for 2 h). The dielectric response of these pellets was measured at 10, 100, and 250 kHz using a Hewlett Packard inductance−capacitance−resistance (LCR) meter. Measurements were carried out in a tube furnace heating the sample at 1 °C min^{-1} to 800 °C. Ferroelectric tests were carried out using a Radiant Technologies RTA60A ferroelectric testing rig with a high-voltage T-REK 609 × 10^{-6} amplifier.

We performed density functional theory (DFT) calculations using the ABINIT package[31] and norm-conserving pseudopotentials generated with the ONCVPSP code.[32] The following orbitals were treated as valence electrons in the pseudopotentials: 2s and 2p for O; 3s, 3p, 3d, and 4s for Ti; 4s, 4p, 4d, and 5s for Nb; 5s, 5p, and 6s for Cs; and 5d, 6s, and 6p Bi. The outer $B(2)$ site ($2g$ in the $P4/mmm$ model, see Figure 3a) is occupied by both Nb and Ti, and so the virtual crystal approximation (VCA)[33] was used to construct an "alchemical" virtual atom made of 50% Nb and 50% Ti for this site. We kept a regular Ti atom for the central $B(1)$ site ($1a$ in the $P4/mmm$ model, see Figure 3a). Testing several exchange correlation functionals on the $P4/mmm$ phase showed that the GGA-PBE functional gives the best agreement between theory and experiments (see SI2). We converged the calculations up to 1 meV/f.u. on energy differences and up to 2 cm^{-1} on phonon frequencies by setting the cutoff energy at 50 Ha for the plane wave expansion and the k-point grid at 6×6×2 for the integration in the Brillouin zone of the $P4/mmm$ phase and at 3×3×2 for phases having a doubling of the unit cell with respect to the $P4/mmm$. The phonon frequencies, Born effective charges, dielectric constants, and piezoelectric coefficients were

Table 1. Structural Parameters for Refinement for CsBi$_2$Ti$_2$NbO$_{10}$ Using 25°C (Backscattered) NPD Data^a

atom	site	x	y	z	occupancy	$U_{iso} \times 100$ (Å^2)
Cs	4b	0.25	0.495(1)	0^b	1^c	1.2(1)
Bi	8c	0.92560(8)	0.5058(5)	−0.040(1)	1^c	2.40(7)
Ti/Nb(1)	4a	0	0	−0.036(3)	0.88(5)/0.12(5)	1.68(3)
Ti/Nb(2)	8c	0.8590(4)	−0.012(4)	0.006(4)	0.56(5)/0.44(5)	1.68(3)
O(1)	8c	0.0059(2)	0.753(1)	0.286(1)	1^c	3.5(1)
O(2)	8c	0.9372(1)	−0.0559(1)	0.047(1)	1^c	2.5(1)
O(3)	8c	0.8687(1)	0.777(1)	0.316(1)	1^c	1.29(9)
O(4)	8c	0.3760(1)	0.728(1)	0.256(1)	1^c	0.25(6)
O(5)	8c	0.8013(1)	0.0301(1)	0.017(1)	1^c	0.55(6)

^{a}Refinement carried out in space group $Ima2$, a = 30.7553(6) Å, b = 5.4451(1) Å, c = 5.4917(1) Å; R_{wp} = 1.33%, R_p = 1.56%, and χ^2 = 3.79. ^{b}Coordinate fixed to define origin along z in space group $Ima2$. ^{c}Parameter fixed in refinements.

Table 2. Selected Bond Angles and Lengths for $Ima2$ Structure of CsBi$_2$Ti$_2$NbO$_{10}$ from Refinement Using NPD Data Collected at 25°C

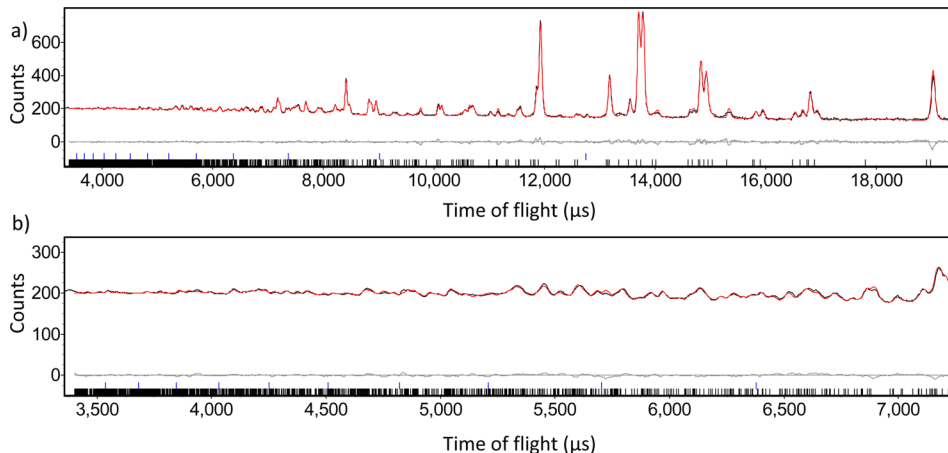|	bond (Å)		bond (Å) or angle
Cs−O(4)	2×3.033(7), 2×3.094(7), 2×3.253(7), 2×3.265(7)	Ti/Nb(1)−O(1)−Ti/Nb(1)	159.6(8)°
Bi−O(3)	1×2.256(6), 1×2.421(7), 1×2.567(7), 1×3.008(7)	Ti/Nb(2)−O(3)−Ti/Nb(2)	153.2(1)°
Bi−O(2)	1×2.31(1), 1×2.460(5), 1×3.116(5), 1×3.26(1)	Ti/Nb(2)−O(2)	1×2.43(1)
Bi−O(1)	1×2.693(8), 1×2.955(7), 1×3.104(8), 1×3.116(5)	Ti/Nb(2)−O(3)	1×1.81(3), 1×2.07(3)
		Ti/Nb(2)−O(4)	1×1.97(3), 1×2.13(3)
Ti/Nb(1)−O(1)	2×1.70(1), 2×2.23(1)	Ti/Nb(2)−O(5)	1×1.79(1)
Ti/Nb(1)−O(2)	2×2.006(6)	Ti/Nb(1)−O(2)−Ti/Nb(2)	156.6(8)°

Figure 2. Rietveld refinement profiles for 25 °C NPD data fitted with $Ima2$ $2c \times \sqrt{2}a \times \sqrt{2}a'$ model. Observed, calculated, and difference profiles are shown in black, red, and gray with upper (vanadium) and lower (main phase) tick marks in blue and black. Upper panel (a) shows whole time-of-flight range, while lower panel (b) shows enlarged low time-of-flight region.

computed through the density functional perturbation theory (DFPT)[34−36] and the polarization through the Berry phase method.[37] We also strongly benefited from the three levels of parallelization (k-points, bands, and fft-grid) implemented in ABINIT.[38]

RESULTS

Room-Temperature Crystal Structure of CsBi$_2$Ti$_2$NbO$_{10}$. High-resolution NPD data collected at 25 °C could not be fitted by the aristotype $P4/mmm$ $a \times a \times c$ unit cell, and reflections consistent with a larger orthorhombic $\sqrt{2}a \times \sqrt{2}a' \times 2c$ unit cell were observed. Systematic absences were consistent with body centered unit cells (e.g., $Imam$ or $Ima2$ $2c_t \times \sqrt{2}a_t' \times \sqrt{2}a_t$ unit cells, (002) ($1\bar{1}0$) ($\bar{1}10$) compared with the $P4/mmm$ structure). Rietveld refinement using a model of $Ima2$ symmetry gives an acceptable fit to the data. This model allows rotation of $B(1)O_6$ and $B(2)O_6$ octahedra around the polar c axis of the $Ima2$ cell (around the $[\bar{1}10]$

direction in the aristotype $P4/mmm$ structure), as well as rotation of $B(2)O_6$ octahedra around the a axis of the $Ima2$ cell (around the [001] direction in the $P4/mmm$ structure).

Using a global temperature factor for all sites, the distribution of Ti and Nb over the two B sites was refined, with a constraint to maintain stoichiometry. This suggested that although Nb preferentially occupies the outer $B(2)$ site, there is some disorder with ~13% of the inner $B(1)$ site occupied by Nb. Ti and Nb have neutron scattering lengths of opposite signs (7.054(3) fm for Nb, −3.438(2) fm for Ti),[39] and this mixed occupancy gives low average scattering for these sites, so their temperature factors were constrained to be the average of those of the other sites in the structure. In subsequent refinements, the Ti−Nb distribution was fixed, and again, average temperature factors were used for these sites. Recent reports on n = 2 DJ phases have highlighted the textured nature of ceramic

samples[17] with some preferred orientation along the direction perpendicular to the layers,[11] and including this in our refinements (along [100] in our case) further improved the fit.

Details from Rietveld refinements are given in Tables 1 and 2, refinement profiles are shown in Figure 2, and the structure is illustrated in Figure 3.
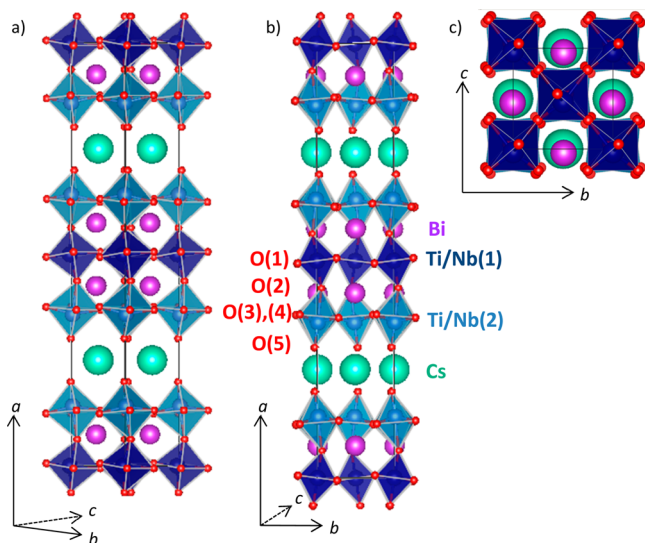

Figure 3. Illustrations of room-temperature crystal structure of $CsBi_2Ti_2NbO_{10}$ described by $Ima2$ symmetry showing Cs, Bi, and Ti/Nb cations in green, purple, and blue, respectively, and $B(1)O_6$ and $B(2)O_6$ octahedra in dark and pale blue.

We note that some Ti/Nb(1)−O bond lengths in this model are fairly short, and this is reflected in high bond valence sum values[40] for these sites (apparent valences of 1.12 and 2.82 are calculated for the Cs and Bi sites, 4.57 and 5.93 for Ti(1) and Nb(1), and 3.86 and 5.00 for Ti(2) and Nb(2), respectively, validating the site preference of Nb^{5+} ions for the $B(2)$ site). As discussed above, the average scattering from these sites is relatively low, so their positions may not be so well determined, and Ti and Nb might be expected to occupy slightly different positions on these sites. However, it is surprising to note that two of these Ti/Nb(1)−O(1) are shorter than the terminal niobyl-like Ti/Nb(2)−O(5) bonds in this model. Some temperature factors are also slightly high (particularly for O(1) and O(2) sites), and it is possible that this reflects some stacking faults in this layered material. However, these short bond lengths and high bond valence sum and U_{iso} values may indicate a deficiency of the model. The nonpolar structure analogous to this $Ima2$ model is of $Imam$ symmetry ($a\bar{c}b$ setting of space group 74) was also considered, and although Pawley fits were equivalent to those for an $Ima2$ cell, Rietveld refinements revealed a significant mismatch in intensities (see SI3). Various related models were also considered, including those that allow similar octahedral rotation about different polar axes (e.g., $Fmm2$, Cc, $C2$, and Cm structures), as well as those with slightly different combinations of octahedral rotation (e.g., nonpolar structures of $Cmca$, $Pbcn$, $P2_1/c$, and $Pnna$ symmetries as well as polar structures of $Abm2$, $Pnc2$, and Pc symmetries). However, these did not give any improvement in fit (and some were noticeably worse) and have large temperature factors and implausibly short bond lengths; refinements using monoclinic models were also particularly unstable. We cannot rule out the possibility of a further

symmetry lowering in this system, but we have been unable to demonstrate this successfully from these data. Higher resolution data might allow lower symmetry models to be considered further and reveal further distortions in $CsBi_2Ti_2NbO_{10}$ that we cannot confirm from our data. The assignment of this $Ima2$ (point group $mm2$) polar, noncentrosymmetric crystal structure is consistent with the clear SHG signal observed at room temperature, indicating that it adopts an acentric structure.[29,41]

Intermediate-Temperature Behavior of $CsBi_2Ti_2NbO_{10}$. On warming up to 545 °C, the splitting associated with the orthorhombic distortion (defined as $2(c - b)/(c + b)$) decreases smoothly, and many of the additional reflections also get weaker (Figure 4). This behavior was followed using sequential refinements using a Pawley cell of $Ima2$ symmetry, and the orthorhombicity and selected peak intensities are shown in Figure 5.
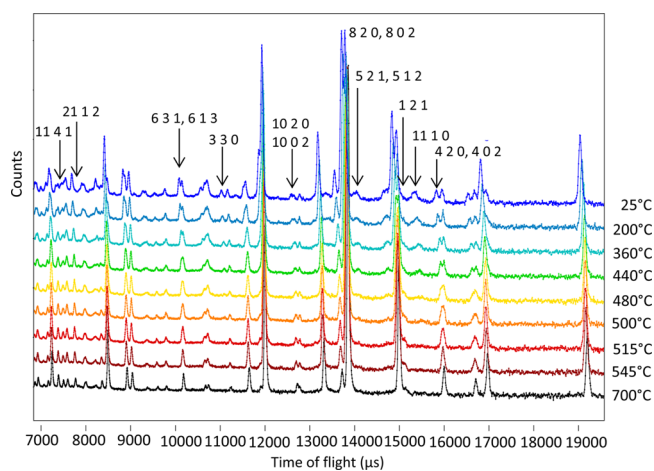

Figure 4. Overlay of NPD data (offset along y) as a function of temperature.

Structures intermediate between the low-temperature $Ima2$ model and the aristotype $P4/mmm$ model were considered for higher temperatures below the orthorhombic−tetragonal phase transition. These included a polar $Amm2$ model ((001) ($1\bar{1}0$) ($\bar{1}\bar{1}0$) compared with $P4/mmm$ cell) and a nonpolar $Imam$ model ((002) ($1\bar{1}0$) ($\bar{1}\bar{1}0$); as above, this $a\bar{c}b$ setting of space group 74 is used for ease of comparison with the low-temperature $Ima2$ model). Reflections consistent with a doubling of the unit cell along the long axis c_t (e.g., 3 3 0, 11 1 0, 1 2 1, Figure 5) are present up to 545 °C, ruling out $Amm2$ models (see SI4 for fits to 515 °C data). Reflection conditions for $Imam$ and $Ima2$ symmetries are identical, but Rietveld refinement of these models suggests a noticeable mismatch in some peak intensities for the $Imam$ model at 515 °C (see SI4 for fits), and so the polar $Ima2$ model seems more plausible below the orthorhombic phase transition.

High-Temperature Behavior of $CsBi_2Ti_2NbO_{10}$. No orthorhombic distortion was observed from data collected at $T \geq 545$ °C, and these patterns could be fitted well by tetragonal cells. Although Pawley fits using the aristotype $P4/mmm$ $a{\times}a{\times}c$ were reasonable, some very weak additional reflections not indexed by this cell were observed to persist up to 700 °C (including hkl $h \neq 2n$ reflections, e.g., 11 2 1 based on $Ima2$ cell, Figures 4 and 5). These reflections can be indexed by tetragonal $\sqrt{2}a_t{\times}\sqrt{2}a_t{\times}2c_t$ cells of $I4/mcm$ symmetry (see
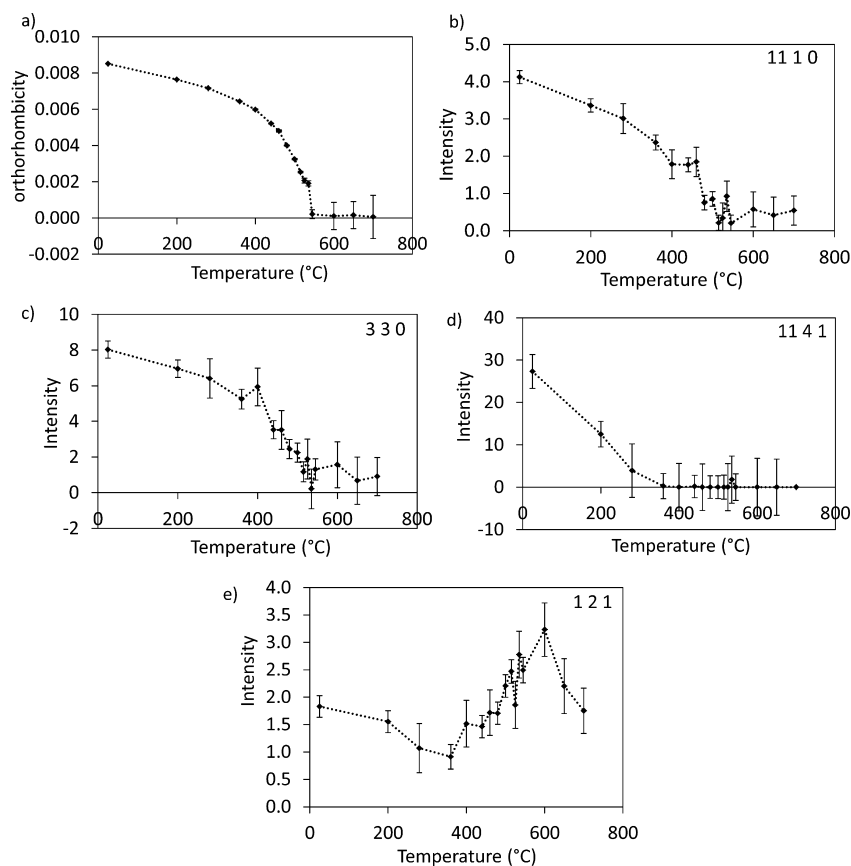
Figure 5. Details from sequential refinements using a Pawley phase of $Ima2$ symmetry ($2c_t \times \sqrt{2}a_t \times \sqrt{2}a_t'$ unit cell) showing orthorhombicity ($2(c - b)/(c + b)$) as well as fitted intensities of several reflections; hkl indices refer to the $Ima2$ cell.

SI7). Models of $I4/mcm$ symmetry can be derived from the aristotype $P4/mmm$ structure by allowing rotation of the BO_6 octahedra around the tetragonal c axis, and for this $n = 3$ DJ phase, there are three possible rotational modes (A1−, A2+, and A3+ irreducible representations, with k-vector ($^1/_2$ $^1/_2$ $^1/_2$)) that would give rise to models of $I4/mcm$ symmetry.

We cannot conclusively distinguish between these very similar models from our data, and the improvement in fit in Rietveld refinements from both these models is minimal (see SI7). We also considered the possibility of a metrically tetragonal model of $Imam$ symmetry allowing A5+ octahedral rotations in this high-temperature region, but this did not give a significantly improved fit and seems unlikely. There may be some concerted rotation of BO_6 octahedra in $CsBi_2Ti_2NbO_{10}$ above 545 °C, but we cannot confirm this from our current data.

DFT Calculations. To identify the patterns of displacements that can lower the symmetry of the high-temperature phase of $CsBi_2Ti_2NbO_{10}$, we calculated the phonon dispersion curves in the aristotype $P4/mmm$ phase (Figure 6). We note that numerous instabilities are present, i.e. numerous patterns of displacements can lower the energy of the $P4/mmm$ phase. A second striking feature is the lack of dispersion between M and A points, and between Z and Γ points, indicating little structural connectivity along $[001]_t$ between successive perovskite blocks (which are separated by large Cs^+ ions).

To identify the ground state we condensed and fully relaxed different combinations of the unstable modes up to the point where no unstable mode remains in the structure. In Figure 7 we present a summary diagram of the relative gain of energy
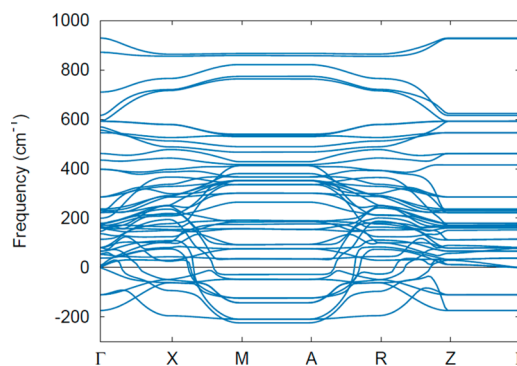

Figure 6. Calculated phonon dispersion curves of the $P4/mmm$ phase of $CsBi_2Ti_2NbO_{10}$. Negative values correspond to imaginary frequencies, i.e., to unstable phonon modes. The coordinates of the high-symmetry points are X ($^1/_2$, 0, 0), M ($^1/_2$, $^1/_2$, 0), A ($^1/_2$, $^1/_2$, $^1/_2$), R ($^1/_2$, 0, $^1/_2$), and Z (0, 0, $^1/_2$).

with respect to the $P4/mmm$ phase for different pathways of mode condensations, and in Table 3 the calculated values.

If we consider only single irrep condensations, we see that the unstable modes that drive the largest energy gain are the polar and antipolar instabilities at the Γ and Z points, i.e., modes involving polar-type displacements in the $[110]_t$ direction. At the Γ point, the Γ5− mode (at 174i cm^{-1}) corresponds to an in-plane ferroelectric instability and gives phases of $Pmm2$ and $Amm2$ symmetries (for polarization along one or two in-plane directions, respectively). At the Z point, the Z5− mode (also at 174i cm^{-1}) corresponds to an in-plane antiferroelectric instability where the sign of the polarization
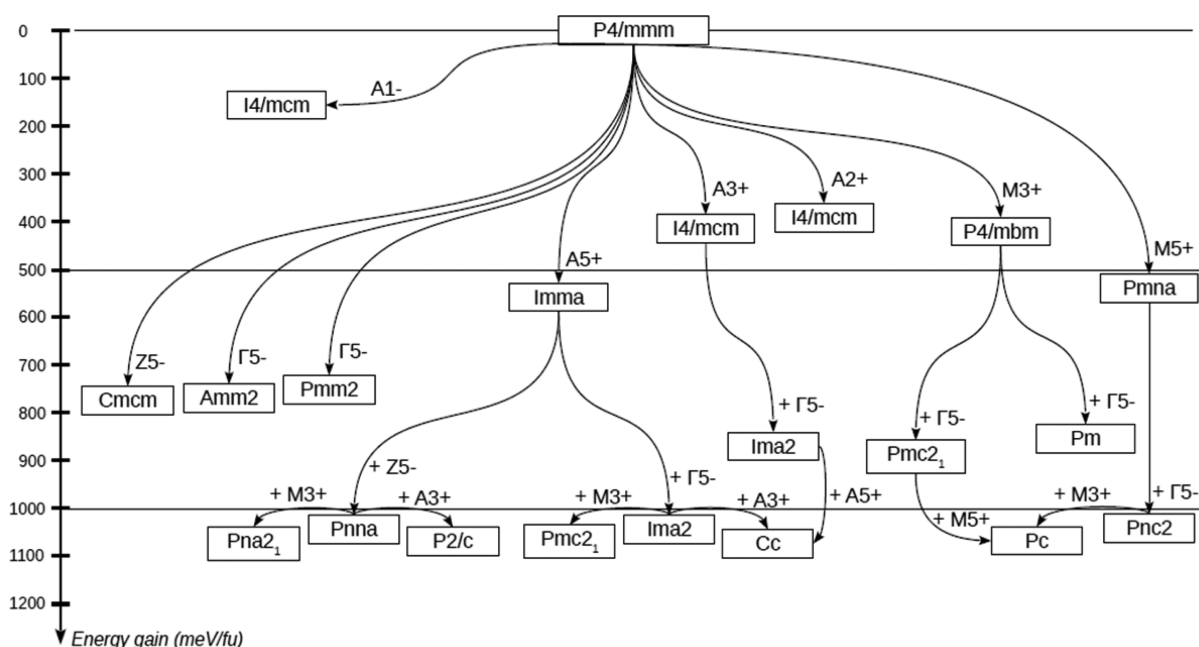
Figure 7. Summary diagram of phases calculated from DFT. The vertical distances give the energy difference (in meV/formula unit) with respect to the $P4/mmm$ phase. Only a selection of the most important connection lines between the phases has been drawn for clarity.

Table 3. Relative Energies of Relaxed Structures of $CsBi_2Ti_2NbO_{10}$ from DFT Calculations[a]

space group	mode condensed	ΔE (meV/f.u.)	mode decomposition (Å)
$Cmcm$	Z5−	788	Z5− (1.17)
$Amm2$	Γ5−	784	Γ5− (0.78), Γ2+ (0.07)
$Pmm2$	Γ5−	755	Γ5− (0.82)
$Imma$	A5+	568	A5+ (1.49)
$Pmna$	M5+	565	M5+ (1.48)
$P4/mbm$	M3+	433	M3+ (1.33)
$I4/mcm$	A3+	423	A3+ (1.31)
$I4/mcm$	A2+	390	A2+ (1.31)
$I4/mcm$	A1−	172	A1− (1.11)
Cc	A5+, Γ5−, A3+	1053	A5+ (1.23), Γ5− (0.93), A1− (0.61), A3+ (0.59), Γ3− (0.22), Γ5+ (0.14), A5− (0.10), A2+ (0.02)
$Pna2_1$	A5+, Z5−, M3+	1053	A5+ (1.74), Z5− (1.50), M1− (0.86), M3+ (0.84), Γ3− (0.31), Z5+ (0.29), A5− (0.14), A2+ (0.03)
Pc	M5+, Γ5−, M3+	1050	M5+ (1.22), Γ5− (0.93), M1− (0.61), M3+ (0.59), Γ3− (0.20), Γ5+ (0.12), M5− (0.09), M2+ (0.02)
$Pmc2_1$	A5+, Γ5−, M3+	1050	A5+ (1.73), Γ5− (1.31), A1− (0.87), M3+ (0.81), Z3− (0.32), Z5+ (0.24), M5− (0.11), M2+ (0.03)
$Ima2$	A5+, Γ5−	1039	A5+ (1.29), Γ5− (0.94), A1− (0.65)
$Pnna$	A5+, Z5−	1039	A5+ (1.82), Z5− (1.46), M1− (0.92)
$Pnc2$	M5+, Γ5−	1038	M5+ (1.28), Γ5− (0.95), M1− (0.65)
$Pmc2_1$	M3+, Γ5−	899	Γ5− (0.94), M3+ (0.86), M5− (0.62), M2+ (0.03)
$Ima2$	A3+, Γ5−	897	Γ5− (0.94), A3+ (0.83), A5− (0.61), A2+ (0.03)
Pm	M3+, Γ5−	846	Γ5− (1.09), M3+ (0.84), M4+ (0.42), M5− (0.20), Γ2+ (0.16)
$Fmm2$	A3+, Γ5−	842	Γ5− (1.09), A3+ (0.84), A4+ (0.43), A5− (0.20), Γ2+ (0.16)

[a]The table is decomposed into two parts: the upper rows show results from single irrep condensations, and the lower rows show results from condensing more than one unstable mode. The first column reports the space group in which the relaxation has been done; the second lists the irrep of the unstable modes that have been condensed into the aristotype $P4/mmm$ structure and that gives the subgroup given in the first column; the third column gives the energy gain driven by condensation of the mode(s) in column 2 followed by a full cell relaxation; the last column gives the mode decomposition of the relaxed structures using the AMPLIMODES software.[42]

alternates between successive perovskite blocks, and gives phases of $Pmma$ and $Cmcm$ symmetries.

The next important unstable modes correspond to out-of-phase rotation of BO_6 octahedra about the in-plane $[110]_t$ direction ($a^-a^-c^0$ in Glazer notation). This rotation can alternate in sign from block to block (A5+ mode) leading to a phase of $Imma$ symmetry (standard setting of $Imam$ model described above), or can be identical from block to block (M5+ mode), leading to a model of $Pmna$ symmetry, with both

modes at 210i cm^{-1}. Instabilities involving rotation of BO_6 octahedra about the out-of-plane $[001]_t$ direction (e.g., A3+, A2+, A1−, or M3+ modes) also give significant energy gains, but not as large as those involving rotation about $[110]_t$. These rotational modes are illustrated in the Supporting Information (SI8).

When considering the condensation of more than one unstable mode, we find that several phases of similar energy can be obtained. For example, condensing the A5+ and Γ5− modes
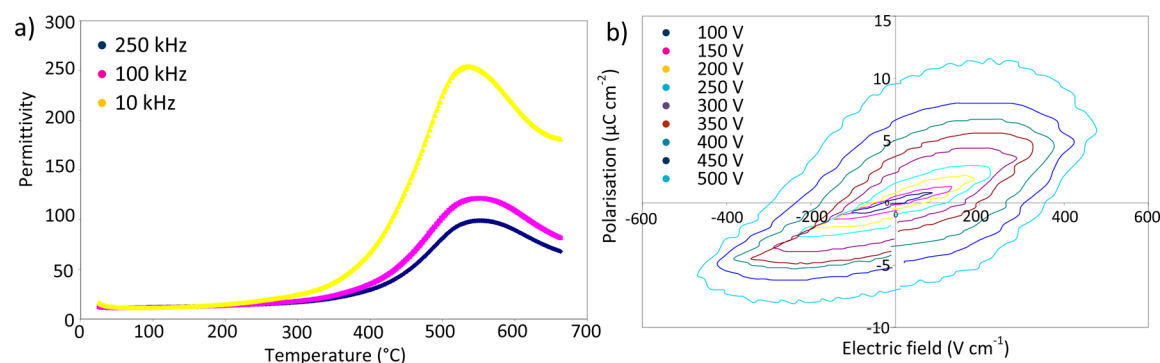
Figure 8. (a) Permittivity ε_r as a function of temperature and frequency for $CsBi_2Ti_2NbO_{10}$. (b) Polarization−electric field measurements at room temperature.

together (*Ima*2 phase) gives an energy gain similar to that obtained by condensing the A5+ and Z5− modes together (*Pnna* phase) or the M5+ and Γ5− modes together (*Pnc*2 phase). Interestingly, each of these three phases has remaining unstable modes such that the ground-state phases are given by more complex mode condensations. For example, *Ima*2 phase has two instabilities which would lower the symmetry to *Pmc*2$_1$ or *Cc*, respectively.

These DFT calculations suggest that the strong polar Γ5− instability (polarization along $[110]_t$) in $CsBi_2Ti_2NbO_{10}$ is consistent with proper ferroelectricity in this $n = 3$ DJ phase. This polar instability develops in the absence of other order parameters and gives a large energy gain. A second, remarkable feature of these results is the number of phases of similar energy, suggesting that metastable phases may exist in this phase diagram, and that the properties of a sample (for example, whether it is polar and ferroelectric, or antiferroelectric) may be sensitive to synthesis routes and annealing conditions, as well as to changes in composition. In particular, the separation of the perovskite blocks, influenced by the *A′* cation, is likely to alter these subtle energy differences, and it would be interesting to investigate the effect of substituting the large Cs$^+$ ions by smaller Rb$^+$ or K$^+$ ions.

Table 3 gives the results of mode decompositions of the relaxed structures obtained using the AMPLIMODE software[42] and shows that condensing more than one mode always drives improper coupling with other modes. This is particularly true for the *Ima*2 phase observed experimentally where the DFT relaxations shows that in addition to the A5+ and Γ5− condensed modes, a third A1− mode develops in the structure. This is confirmed by symmetry analysis where the trilinear term A5+⊗Γ5−⊗A1− is an invariant of the energy expansion around the *P*4/*mmm* phase. We note that the A5+ and Γ5− instabilities are fairly strong, while the A1− instability is much weaker. Given the strength of the polar Γ5− instability, it is unlikely that this polarization is driven by the trilinear coupling, suggesting that hybrid-improper mechanisms for ferroelectricity may not be relevant in $CsBi_2Ti_2NbO_{10}$. Similar improper coupling occurs in the other low symmetry phases, the most striking of which are perhaps the ground state *Cc* and *Pna*2$_1$ phases where an improper coupling activates the polar Γ3− mode with polarization in the $[001]_t$ direction. Since the Γ3− mode is not unstable in the *P*4/*mmm* phase, we can conclude that the *Cc* phase is a proper ferroelectric in the $[110]_t$ direction and is an improper ferroelectric in the $[001]_t$ direction. We note that since this phase is connected to the experimental *Ima*2 phase at 25 °C, these results suggest that the *Cc* phase

might be observed experimentally at lower temperature. We have calculated the piezoelectric response of the *Cc* and *Pc* phases and found that the in-plane components d$_{22}$ (17 pC/N) and d$_{61}$ (34 pC/N) are the largest components. These are larger than those reported for the $n = 2$ phases (regardless of direction), although we d$_{33}$ value is smaller for $CsBi_2Ti_2NbO_{10}$ (4 pC/N for the *Cc* phase, −2 pC/N for the *Pc* phase), compared with $RbBiNb_2O_7$ (13 pC/N).[16]

Electrical Characterization of $CsBi_2Ti_2NbO_{10}$. Measurements of the dielectric response of $CsBi_2Ti_2NbO_{10}$ (Figure 8a) show that the sample has a low permittivity (similar to that reported recently for $RbBiNb_2O_7$[14] and $CsBiNb_2O_7$[10]) but that is temperature dependent, increasing to a maximum just below 550 °C. Improper ferroelectrics typically show temperature-independent permittivity.[43] Our temperature-dependent data are therefore more consistent with a proper ferroelectric−paraelectric phase transition, although the low permittivity values may reflect the low density of the ceramic. Polarization-field measurements were carried out to test for ferroelectricity and are shown in Figure 8b. Polarization saturation is not observed at high fields for this sample, and these measurements suggest the sample is electrically "leaky" (bulk resistance of 6 × 10^6 Ωcm at room temperature). Again, this is consistent with the high porosity of the ceramic used, due to the low sintering temperature. It would be of interest to test for any piezoelectric activity in future studies.

Optical Characterization. Diffuse reflectance measurements for $CsBi_2Ti_2NbO_{10}$ diluted in NaCl show a decrease in reflectance from 440 nm. The diffuse reflectance spectrum for $CsBi_2Ti_2NbO_{10}$ after the Kubelka−Munk treatment is shown in Figure 9. The intercept of the linear increase in the Kubelka−Munk remission function $F = (1 − R)^2/2R$ (where R is the
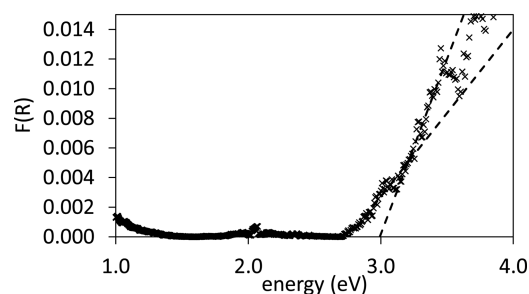

Figure 9. Diffuse reflectance spectrum for $CsBi_2Ti_2NbO_{10}$ diluted in dry NaCl after Kubelka−Munk treatment showing the band gap in the visible region.

diffuse reflectance) with the energy axis can be used to determine the optical band gap.[30,44] These data suggest an optical band gap of 3.0(1) eV for $CsBi_2Ti_2NbO_{10}$, with a lower energy feature immediately below the band gap (possibly an exciton) also observed. This is very similar to the optical behavior reported for $CsBiNb_2O_7$.[45]

■ DISCUSSION

The structural behavior described here is similar to that observed for $n = 3$ Aurivillius materials,[46,47] and consistent with a ferroelectric−paraelectric phase transition at ∼540 °C observed in electrical measurements (despite the leaky nature of the ceramics).

The B sites in the perovskite blocks are occupied by the d^0 cations Ti^{4+} and Nb^{5+}, with the larger Nb^{5+} cation (6-coordinate ionic radius 0.64 Å, compared with 0.605 Å for Ti^{4+})[48] preferentially occupying the lower symmetry $B(2)$ site which is slightly larger than the $B(1)$ site. A major driving force for the octahedral rotations (and resulting orthorhombic distortion) is likely to be the optimization of bonding around the nonspherical Bi^{3+} cation with its stereochemically active lone pair. The orthorhombicity observed here for $CsBi_2Ti_2NbO_{10}$ (8.5×10^{-3}, Figure 5a) is less than that for $CsBiNb_2O_7$ (13.5×10^{-3}),[11] perhaps reflecting the presence of the smaller Ti^{4+} cations, suggesting that tolerance factor arguments might also be relevant: the tolerance factor for the $Bi_2Ti_2NbO_{10}$ blocks in $CsBi_2Ti_2NbO_{10}$ is slightly smaller than for the perovskite blocks in $Bi_4Ti_3O_{12}$ which has an orthorhombicity of 6.6×10^{-3}.[47] Despite these distortions, the $B(1)$ cations are noticeably overbonded in our $Ima2$ model, while Bi sites are slightly underbonded. It is likely that the alkali interlayers also influence the bonding environment. As Cs^+ is replaced by smaller Rb^+ in the $n = 2$ phases $ABiNb_2O_7$ (A = Cs, Rb), there is a significant contraction in the ab plane[17] suggesting that in $CsBi_2Ti_2NbO_{10}$, the large Cs^+ ion (already slightly overbonded), limits the lattice distortion, forcing a larger in-plane width and leaving the Bi and $B(2)$ sites underbonded.

The cations in the low-temperature structure of $CsBi_2Ti_2NbO_{10}$ are noticeably displaced from the centers of their coordination environments (Figure 10). The outer $B(2)$ sites are displaced toward the apical oxide site next to the alkali interl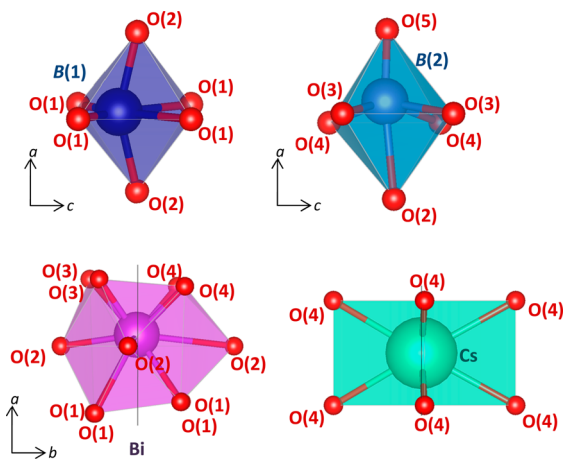ayer, and this out-of-center displacement persists up to at least 700 °C (see Table SI6:2), presumably to compensate for the slight underbonding of this site. There are also significant displacements along the polar [001] direction (Figure 11), and the polarization is 39(2) $\mu C\ cm^{-2}$ at 25 °C (calculated using a simple point charge model),[49] and 49 $\mu C\ cm^{-2}$ from our DFT calculations, similar to values calculated for $CsBiNb_2O_7$ (22.9 $\mu C\ cm^{-2}$)[11] and $Bi_4Ti_3O_{12}$ (28 $\mu C\ cm^{-2}$).[50] This polarization results mainly from Bi and the equatorial O(3) sites. However, there is also a sizable displacement of both B sites along this polar axis (in opposite directions). This is in agreement with our DFT results and with results from recent first-principles calculations which show significant polar displacement of B site cations in $n = 2$ DJ phases, which provides the major contribution to the polarization in these materials.[21] This is in contrast to most other families of layered perovskite-related materials[4] and might explain the difficulties in introducing magnetic d^n ions onto the DJ B sites,[51] in contrast to other systems such as the Aurivillius materials.[13,52−58]

DFT calculations show that the aristotype $P4/mmm$ structure is most vulnerable to distortions involving octahedral rotation about $[110]_t$, suggesting that the high-temperature phase is less likely to undergo symmetry-lowering phase transitions via an intermediate phase of $I4/mcm$ symmetry. The derivation of the low-temperature $Ima2$ model from the aristotype $P4/mmm$ structure can be understood in terms of group−subgroup relations (Figure 12) with the polar Γ5− displacive and A5+ tilt distortion modes being significant for this symmetry lowering.

The low-temperature $Ima2$ structure is characterized by ferroelectric displacements along the polar [001] direction (the Γ5− irrep) and rotations of $B(1)O_6$ and $B(2)O_6$ octahedra about this polar axis ($a^-a^-c^0$ in Glazer notation, described by the A5+ irrep); angles between equatorial planes of $B(1)O_6$ octahedra and $B(2)O_6$ octahedra at 25 °C are 164.8(2)° and 163.5(2)°, respectively. There is also a small rotation of $B(2)O_6$ octahedra about the long axis of 6.9(1)° (in Glazer notation $a^0a^0c^-$ within the blocks, but in-phase from block to block, described by the A1− irrep). This is similar to the results of DFT and NMR studies of $RbSr_2Nb_3O_{10}$ which considered various octahedral rotation modes and suggested rotations of different magnitudes for the inner and outer NbO_6 octahedra around the c axis, although we note that the relative magnitudes of rotation are opposite in $RbSr_2Nb_3O_{10}$ to those in $CsBi_2Ti_2NbO_{10}$ (inner octahedra rotate by 14(1)° and outer octahedra by −3(1)° in $RbSr_2Nb_3O_{10}$).[59] The rotation pattern in $CsBi_2Ti_2NbO_{10}$ is analogous to the tilt system described by Rae et al. for the $n = 3$ Aurivillius phase $Bi_4Ti_3O_{12}$ at room temperature, who illustrated that the coexistence of the polar displacement (the Γ5− distortion mode) and the octahedral rotation around this polar direction (A5+ distortion mode) implies the possible coexistence of rotation of $B(2)O_6$ octahedra around the long axis (A1− distortion mode here).[60] Figure 13 shows unit cell parameters and the amplitudes of the Γ5− displacive mode on the Bi site, A1− and A5+ rotational modes, and calculated polarization (below phase transition) as a function of temperature. These results are from sequential distortion mode refinements of an $Ima2$ model, with peak shape terms and Cs Γ5− mode amplitude fixed, as well as constraints applied to minimize octahedral distortions (e.g., apical O(2) and O(4) sites to tilt by the same amount). These results suggest that the polar Γ5− mode and A5+ tilt modes become active simultaneously. (We emphasize that at high temperatures, the A1− tilt gives a negligible improvement

Figure 10. Illustration of the coordination environments of B(1), B(2), Bi, and Cs cations in $CsBi_2Ti_2NbO_{10}$ at 25 °C.
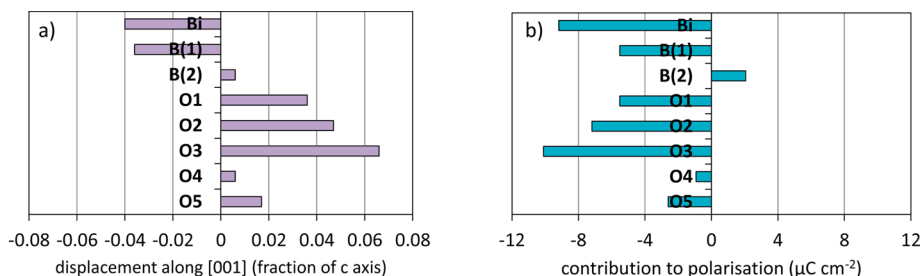
Figure 11. Schematic drawings of (a) atomic displacements (fraction of the c axis length) and (b) contributions to the total ferroelectric polarization ($\mu C\ cm^{-2}$) of each ion of $CsBi_2Ti_2NbO_{10}$ at 25 °C. The position of Cs on the c axis is fixed at the origin.
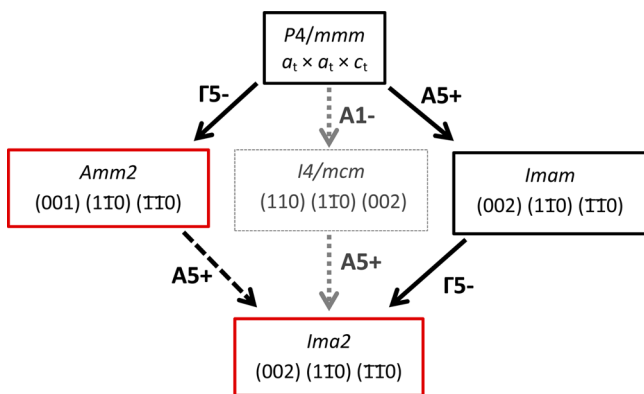

Figure 12. Group–subgroup relations showing derivation of polar $Ima2$ model from aristotype $P4/mmm$ model with polar models highlighted with solid red lines, nonpolar models with dashed black lines.

in fit, and DFT calculations indicate only a small energy gain for this distortion, so it is unlikely to be active for $T > 545$ °C.)

It is interesting to consider the possible sequence of phase transitions on cooling $CsBi_2Ti_2NbO_{10}$, particularly in the light of recent studies of hybrid-improper ferroelectrics, in which two nonpolar lattice distortions (such as octahedral rotational modes) give rise to a polar structure.[22,61] These mechanisms are well understood for the $n = 2$ DJ phases $AA'Nb_2O_7$ in which the combination of an M2+ rotational mode ($a^0a^0c^+$) and an M5− rotational mode ($a^-a^-c^0$) lowers the symmetry to $P2_1am$, in which the polar Γ5− displacive mode is trilinearly coupled with these M2+ and M5− rotational modes; only with both rotational modes active does the Γ5− displacive mode lower the free energy further.[21]

In this $n = 3$ DJ phase, rotation of BO_6 octahedra about the polar axis doubles the unit cell along the long axis (due to the mirror plane at $x = 0.25$), corresponding to the A5+ irrep, but otherwise is similar to the M5− rotation in the $n = 2$ phases. Rotation about the long axis is more complicated for these odd-n DJ phases. As highlighted by Benedek, combinations of analogous rotational modes involving both inner $B(1)O_6$ and outer $B(2)O_6$ octahedra for odd-n DJ phases would result in nonpolar structures (see SI9).[21]

We note that our room-temperature model of $Ima2$ symmetry allows both A5+ rotation ($a^-a^-c^0$) of $B(1)O_6$ and $B(2)O_6$, as well as A1− rotation of $B(2)O_6$ octahedra. This A1− rotation involves rotation of the outer $B(2)O_6$ octahedra around the tetragonal axis (out-of-phase within a perovskite block, in-phase between blocks). This A1− distortion seems surprising, and DFT calculations show that, for the aristotype $P4/mmm$ phase, this distortion gives a fairly high energy phase

(Figure 7 and Table 3). Nevertheless, it is analogous to that observed in $Bi_4Ti_3O_{12}$.[60] In light of the recent work on the hybrid-improper mechanism, it is tempting to speculate that a similar mechanism, involving A5+ and A1− rotations, gives rise to the polar, ferroelectric $Ima2$ phase of $CsBi_2Ti_2NbO_{10}$ (see central greyed out chain in Figure 12). We see no evidence of intermediate phases of $Imam$ ($Imma$) or $Amm2$ symmetry for $CsBi_2Ti_2NbO_{10}$, suggesting that, in this case, the A5+ and Γ5− modes condense at the same temperature.

In proper ferroelectrics, the primary driving force for the paraelectric−ferroelectric phase transition is the polar instability, while in (hybrid)-improper ferroelectrics, the polarization is induced by other order parameter(s) and would otherwise be absent. In $CsBi_2Ti_2NbO_{10}$, the strong Γ5− and A5+ instabilities appear to condense at the same temperature, and symmetry analysis shows that a trilinear coupling between these two modes and the A1− mode is allowed, consistent with an improper character of the transition. However, the strength of the polar Γ5− instability and the weakness of the A1− instability in the DFT calculations point toward $CsBi_2Ti_2NbO_{10}$ behaving like a proper ferroelectric. The exact character of this transition thus calls for careful phonon analysis around the phase transition and further computational studies. This result is consistent with the temperature dependence of dielectric permittivity (Figure 8a). It is striking that increasing the width of the perovskite block from the $n = 2$ phase $CsBiNb_2O_7$ to the $n = 3$ $CsBi_2Ti_2NbO_{10}$ stabilizes this proper ferroelectricity, and further studies to understand the origin of this stabilization are needed.

Some disorder of oxide sites has been reported for $CsLa_2Ti_2NbO_{10}$,[19] and although no polar behavior has been reported for this material, the solid solution $CsLa_{2-x}Bi_xTi_2NbO_{10}$ described above might allow relaxor ferroelectric materials to be prepared. Further investigations of the role of the A cation in these systems using neutron powder diffraction and electron diffraction are underway. For the even-n Aurivillius phases, Hyatt et al.[62] and Giddings et al.[57] have correlated the existence of intermediate nonpolar phases (with BO_6 rotation about $[110]_t$ only) with orthorhombic strain (due to interfacial bond length mismatch). It would be interesting to extend this analysis to the DJ family. $RbLaNb_2O_7$ adopts a nonpolar $Imma$ structure with octahedral rotation about $[110]_t$ with only slight orthorhombicity (0.3×10^{-3} at room temperature),[63] suggesting that this hypothesis might also give insight into the DJ family and factors that determine whether the $[110]_t$ rotational mode will condense at higher temperatures than further distortions (e.g., $[001]_t$ rotational modes and ferroelectric displacements) forming intermediate, nonpolar phases, or whether these modes will occur simultaneously.
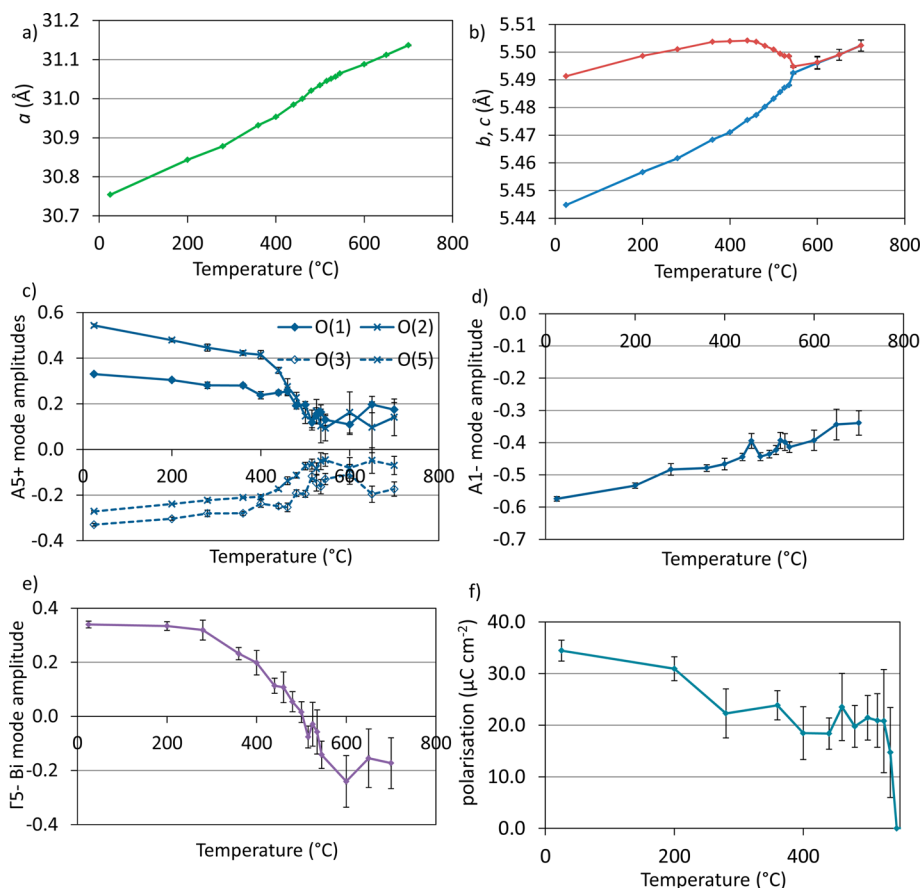
Figure 13. Results from sequential distortion mode refinements for $CsBi_2Nb_2TiO_{10}$ using variable-temperature NPD data showing (a) a unit cell parameter, (b) b (blue) and c (red) unit cell parameters, (c) amplitudes of A5+ modes that describe rotation of BO_6 octahedra about the polar c axis (solid lines for $B(1)O_6$, dashed lines for $B(2)O_6$; apical and equatorial sites represented by diamonds and crosses, respectively), (d) amplitude of A1− rotational mode (rotation of $B(2)O_6$ around long axis), (e) amplitude of polar Γ5− mode on Bi site, and (f) calculated polarization below transition temperature T_C. The peak shape was fixed, the Cs z coordinate was fixed to define the origin along z, and constraints were applied to minimize distortion of the octahedra in these sequential refinements.

CONCLUSIONS

In summary, property measurements and structural studies using variable-temperature NPD data indicate that $CsBi_2Ti_2NbO_{10}$ adopts a polar, ferroelectric structure below 545 °C. DFT calculations give insight into the relative energies of various structural instabilities for this $n = 3$ DJ phase and have been essential for confirming the proper ferroelectric nature of $CsBi_2Ti_2NbO_{10}$, but also suggest that further low-temperature phases may exist with an improper ferroelectric effect. This investigation demonstrates that the $n = 3$ DJ phases differ in their structural chemistry and ferroelectric behavior from the closely related $n = 2$ DJ phases; the key driver is a polar mode itself, and not the secondary coupling of this to two nonpolar (tilt) modes, which has been shown to occur in many of the new generation of layered perovskite ferroelectrics. This is a significant result, and opens up the field to further experimental and theoretical study. The phase diagram of the $n = 3$ phases is likely to be complex; investigations of the influence of A' and A cation size are currently underway.

ASSOCIATED CONTENT

ⓢ Supporting Information

The Supporting Information is available free of charge on the ACS Publications website at DOI: 10.1021/acs.chemmater.5b03564.

SI1, investigation of $CsLa_{2−x}Bi_xTi_2NbO_{10}$ solid solution; SI2, comparison between experimental and DFT structures; SI3, 25 °C NPD data fitted with *Imma* model; SI4, 515 °C NPD data; SI5, 700 °C NPD data; SI6, Rietveld fit for *P4/mmm* model to 700 °C data; SI7, *I4/mcm* models for high-temperature structure; SI8, schematic illustrating octahedral rotation modes for this $n = 3$ DJ phase; SI9, group−subgroup relations for various models derived from the aristotype *P4/mmm* model by combinations of octahedral rotations of both $B(1)O_6$ and $B(2)O_6$ octahedra, including SI figures and tables PDF)

AUTHOR INFORMATION

Corresponding Authors
*E-mail: e.e.mccabe@kent.ac.uk.
*E-mail: n.c.hyatt@sheffield.ac.uk.

Notes
The authors declare no competing financial interest.

ACKNOWLEDGMENTS

■ REFERENCES

(1) de Araujo, C. A.-P.; Cuchiaro, J. D.; McMillan, L. D.; Scott, M. C.; Scott, J. F. Fatigue-free ferroelectric capacitors with platinum electrodes. *Nature* **1995**, *374*, 627−629.

(2) Noguchi, T.; Hase, T.; Miyasaka, Y. Sr0.85Bi2.1Ta2O9. *Jpn. J. Appl. Phys. Part 1* **1996**, *35*, 4900.

(3) Scott, J. F. Applications of modern ferroelectrics. *Science* **2007**, *315* (5814), 954−959.

(4) Benedek, N. A.; Rondinelli, J. M.; Djani, H.; Ghosez, P.; Lightfoot, P. Understanding ferroelectricity in layered perovskites: new ideas and insights from theory and experiments. *Dalton Trans.* **2015**, *44*, 10543−10558.

(5) Aleksandrov, K. S. Structural phase transitions in layered perovskite-like crystals. *Kristallografiya* **1995**, *40*, 279−301.

(6) Aleksandrov, K. S.; Beznosikov, B. V.; Misyul, S. V. Successive phase transitions in crystals of K2MgF4-type structure. *Phys. Status Solidi* **1987**, *104*, 529−543.

(7) Hatch, D. M.; Stokes, H. T. Classification of octahedral tilting phases in the perovskite-like A2BO4 structure. *Phys. Rev. B: Condens. Matter Mater. Phys.* **1987**, *35*, 8509.

(8) Hatch, D. M.; Stokes, H. T.; Aleksandrov, K. S.; Misyul, S. V. Phase transitions in the perovskite-like A2BO4 structure. *Phys. Rev. B: Condens. Matter Mater. Phys.* **1989**, *39*, 9282−9288.

(9) Fennie, C. J.; Rabe, K. M. Ferroelectricity in the Dion-Jacobson CsBiNb2O7 from first principles. *Appl. Phys. Lett.* **2006**, *88*, 262902.

(10) Goff, R. J.; Keeble, D.; Thomas, P. A.; Ritter, C.; Morrison, F. D.; Lightfoot, P. Leakage and proton conductivity in the predicted ferroelectric CsBiNb2O7. *Chem. Mater.* **2009**, *21*, 1296−1302.

(11) Snedden, A.; Knight, K. S.; Lightfoot, P. Structural distortions in layered perovskites CsANb2O7. *J. Solid State Chem.* **2003**, *173*, 309−313.

(12) Hervoches, C. H.; Irvine, J. T. S.; Lightfoot, P. Two high temperature paraelectric phases in Sr0.85Bi2.1Ta2O9. *Phys. Rev. B: Condens. Matter Mater. Phys.* **2001**, *64*, 100102(R).

(13) Snedden, A.; Hervoches, C. H.; Lightfoot, P. Ferroelectric phase transitions in SrBi2Nb2O9 and Bi5Ti3FeO15: A powder neutron diffraction study. *Phys. Rev. B: Condens. Matter Mater. Phys.* **2003**, *67*, 092102.

(14) Li, B.-W.; Osada, M.; Ozawa, T. C.; Sasaki, T. RbBiNb2O7: a new lead-free high TC ferroelectric. *Chem. Mater.* **2012**, *24*, 3111−3113.

(15) Sim, H.; Kim, B. G. Octahedral tilting and ferroelectricity in RbANb2O7 (A = Bi, Nd) from first principles. *Phys. Rev. B: Condens. Matter Mater. Phys.* **2014**, *89*, 144114.

(16) Gou, G.; Shi, J. Piezoelectricity enhancement in Dion-Jacobson RbBiNb2O7 via negative pressure. *EPL* **2014**, *108*, 67006.

(17) Chen, C.; Ning, H.; Lepadatu, S.; Cain, M.; Yan, H.; Reece, M. J. Ferroelectricity in Dion-Jacobson ABiNb2O7 (A = Rb, Cs) compounds. *J. Mater. Chem. C* **2015**, *3*, 19−22.

(18) Kurzman, J. A.; Geselbracht, M. J. Probing octahedral tilting in Dion-Jacobson layered perovskites with neutron powder diffraction and Raman spectroscopy. *Mater. Res. Soc. Symp. Proc.* **2007**, *988*, 0988-QQ08-06.

(19) Hong, Y.-S.; Kim, S.-J.; Kim, S.-J.; Choy, J.-H. B-site cation arrangement and crystal structure of layered perovskite compounds CsLn2Ti2NbO10 (Ln ~ La, Pr, Nd, Sm) and CsCaLaTiNb2O10. *J. Mater. Chem.* **2000**, *10*, 1209−1214.

(20) Thangadurai, V.; Schmid-Beurmann, P.; Weppner, W. Synthesis, structure and electrical conductivity of A'[A2B3O10] (A' = Rb, Cs; A = Sr, Ba; B = Nb, Ta): new members of Dion-Jacobson-type layered perovskites. *J. Solid State Chem.* **2001**, *158*, 279−289.

(21) Benedek, N. A. Origin of ferroelectricity in a family of polar oxides: the Dion-Jacobson phases. *Inorg. Chem.* **2014**, *53*, 3769−3777.

(22) Benedek, N. A.; Fennie, C. J. Hybrid improper ferroelectricity: a mechanism for controllable polarization-magnetization coupling. *Phys. Rev. Lett.* **2011**, *106*, 107204.

(23) Rietveld, H. M. A profile refinement method for nuclear and magnetic structures. *J. Appl. Crystallogr.* **1969**, *2*, 65.

(24) Coelho, A. A. Topas. *J. Appl. Crystallogr.* **2003**, *36*, 86.

(25) Coelho, A. A. *Topas Academic: General profile and structure analysis software for powder diffraction data*; Bruker AXS: Karlsruhe, Germany, 2012.

(26) Campbell, B. J.; Stokes, H. T.; Tanner, D. E.; Hatch, D. M. ISODISTORT. *J. Appl. Crystallogr.* **2006**, *39*, 607−614.

(27) Dollase, W. A. Correction of intensities for preferred orientation in powder diffractometry: application of the March model. *J. Appl. Crystallogr.* **1986**, *19*, 267−272.

(28) March, A. Mathematische Theorie der Regelung nach der Korngestalt bei affiner Deformation. *Z. Kristallogr. - Cryst. Mater.* **1932**, *81*, 285−297.

(29) Ok, K. M.; Chi, E. O.; Halasyamani, P. S. Bulk characterization methods for non-centrosymmetric materials: second-harmonic generation, piezoelectricity, pyroelectricity, and ferroelectricity. *Chem. Soc. Rev.* **2006**, *35*, 710−717.

(30) Kortum, G.; Braun, W.; Herzog, G. Principles and techniques of diffuse reflectance spectroscopy. *Angew. Chem., Int. Ed. Engl.* **1963**, *2*, 333−404.

(31) Gonze, X.; Amadon, B.; Anglade, P. M.; Beuken, J. M.; Bottin, F.; Boulanger, P.; Bruneval, F.; Caliste, D.; Caracas, R.; Côté, M.; Deutsch, T.; Genovese, L.; Ghosez, P.; Giantomassi, M.; Goedecker, S.; Hamann, D. R.; Hermet, P.; Jollet, F.; Jomard, G.; Leroux, S.; Mancini, M.; Mazevet, S.; Oliveira, M. J. T.; Onida, G.; Pouillon, Y.; Rangel, T.; Rignanese, G. M.; Sangalli, D.; Shaltaf, R.; Torrent, M.; Verstraete, M. J.; Zerah, G.; Zwanziger, J. W. ABINIT: First-principles approach to material and nanosystem properties. *Comput. Phys. Commun.* **2009**, *180*, 2582−2615.

(32) Hamann, D. R. Optimized norm-conserving Vanderbilt pseudopotentials. *Phys. Rev. B: Condens. Matter Mater. Phys.* **2013**, *88*, 085117.

(33) Bellaiche, L.; Vanderbilt, D. Virtual crystal approximation revisited: Application to dielectric and piezoelectric properties of perovskites. *Phys. Rev. B: Condens. Matter Mater. Phys.* **2000**, *61*, 7877−7882.

(34) Gonze, X.; Lee, C. Dynamical matrices, Born effective charges, dielectric permittivity tensors, and interatomic force constants from density-functional perturbation theory. *Phys. Rev. B: Condens. Matter Mater. Phys.* **1997**, *55*, 10355−10368.

(35) Wu, X.; Vanderbilt, D.; Hamann, D. R. Systematic treatment of displacements, strains, and electric fields in density-functional perturbation theory. *Phys. Rev. B: Condens. Matter Mater. Phys.* **2005**, *72*, 035105.

(36) Hamann, D. R.; Rabe, K. M.; Vanderbilt, D. Generalized-gradient-functional treatment of strain in density-functional perturbation theory. *Phys. Rev. B: Condens. Matter Mater. Phys.* **2005**, *72*, 033102.

(37) King-Smith, R. D.; Vanderbilt, D. Theory of polarization of crystalline solids. *Phys. Rev. B: Condens. Matter Mater. Phys.* **1993**, *47*, 1651−1654.

(38) Bottin, F.; Leroux, S.; Knyazev, A.; Zérah, G. Large-scale ab initio calculations based on three levels of parallelization. *Comput. Mater. Sci.* **2008**, *42*, 329−336.

(39) Sears, V. F. Neutron scattering lengths and cross sections. *Neutron news* **1992**, *3*, 26−37.

(40) Brown, I. D.; Altermatt, D. Bond-valence parameters obtained from a systematic analysis of the inorganic crystal structure database. *Acta Crystallogr., Sect. B: Struct. Sci.* **1985**, *B41*, 244−247.

(41) Halasyamani, P. S.; Poeppelmeier, K. R. noncentrosymmetric point groups. *Chem. Mater.* **1998**, *10*, 2753−2769.

(42) Orobengoa, D.; Capillas, C.; Aroyo, M. I.; Perez-Mato, J. M. AMPLIMODES: symmetry-mode analysis on the Bilbao crystallography server. *J. Appl. Crystallogr.* **2009**, *42*, 820−833.

(43) Levanyuk, A. P.; Sannikov, D. G. Improper ferroelectrics. *Usp. Fiz. Nauk* **1974**, *112*, 561−589.

(44) Tandon, S. P.; Gupta, J. P. Measurement of Forbidden Energy Gap of Semiconductors by Diffuse Reflectance Technique. *Phys. Status Solidi B* **1970**, *38*, 363−366.

(45) Kim, H. G.; Yoo, J. S.; Ok, K. M. SHG and PL properties of noncentrosymmetric layered perovskite solid solutions $CsBi_{1-x}Eu_xNb_2O_7$. *J. Mater. Chem. C* **2015**, *3*, 5625.

(46) Zhou, Q.; Kennedy, B. J.; Howard, C. J. Structural studies of the ferroelectric phase transition in $Bi_4Ti_3O_{12}$. *Chem. Mater.* **2003**, *15*, 5025−5028.

(47) Hervoches, C. H.; Lightfoot, P. A variable temperature powder neutron diffraction study of ferroelectric $Bi_4Ti_3O_{12}$. *Chem. Mater.* **1999**, *11*, 3359−3364.

(48) Shannon, R. D. Revined effective ionic radii and systematic studies of interatomic distances in halides and chalcogenides. *Acta Crystallogr., Sect. A: Cryst. Phys., Diffr., Theor. Gen. Crystallogr.* **1976**, *A32*, 751.

(49) Shimakawa, Y.; Kubo, Y.; Nakagawa, Y.; Goto, S.; Kamiyama, T.; Asano, H.; Izumi, F. Crystal structure and ferroelectric properties of $ABi_2Ta_2O_9$ (A = Ca, Sr, Ba). *Phys. Rev. B: Condens. Matter Mater. Phys.* **2000**, *61*, 6559−6564.

(50) Dorrian, J. F.; Newnham, R. E.; Smith, D. K.; Kay, M. I. Crystal structure of $Bi_4Ti_3O_{12}$. *Ferroelectrics* **1972**, *3*, 17−27.

(51) Hong, Y.-S. Reinvestigation of Dion-Jacobson phases $CsCa_2b_2MO_9$ (M = Fe, Al). *Bull. Korean Chem. Soc.* **2006**, *27*, 853−856.

(52) McCabe, E. E.; Greaves, C. Structural and magnetic characterisation of $Bi_2Sr_{1.4}La_{0.6}Nb_2MnO_{12}$ and its relationship to $Bi_2Sr_2Nb_2MnO_{12}$. *J. Mater. Chem.* **2005**, *15*, 177−182.

(53) McCabe, E. E.; Greaves, C. Structural and magnetic characterisation of Aurivillius material $Bi_2Sr_2Nb_{2.5}Fe_{0.5}O_{12}$. *J. Solid State Chem.* **2008**, *181*, 3051−3056.

(54) Hervoches, C. H.; Snedden, A.; Riggs, R.; Kilcoyne, S. H.; Manuel, P.; Lightfoot, P. Structural behaviour of the four-layer Aurivillius phase ferroelectrics $SrBi_4Ti_4O1$ and $Bi_5Ti_3FeO_{15}$. *J. Solid State Chem.* **2002**, *164*, 280−291.

(55) Yu, W. J.; Kim, Y. I.; Ha, D. H.; Lee, J. H.; Park, Y. K.; Seong, S.; Hur, N. H. A new manganese oxide with the Aurivillius structure: $Bi_2Sr_2Nb_2MnO_{12-\delta}$. *Solid State Commun.* **1999**, *111*, 705.

(56) Sharma, N.; Ling, C. D.; Wrighter, G. E.; Chen, P. Y.; Kennedy, B. J.; Lee, P. L. Three-layer Aurivillius phases containing magnetic transition metal cations $Bi_{2−2x}Sr_{2+x}(Nb,Ta)_{2+x}M1_{-x}O12$ M = Ru4+, Ir4+, Mn4+. *J. Solid State Chem.* **2007**, *180*, 370−376.

(57) Giddings, A. T.; Stennett, M. C.; Reid, D. P.; McCabe, E. E.; Greaves, C.; Hyatt, N. C. Synthesis, structure and characterisation of the n = 4 Aurivillius phase $Bi_5Ti_3CrO_{15}$. *J. Solid State Chem.* **2011**, *184*, 252−263.

(58) Sharma, N.; Kennedy, B. J.; Elcombe, M. M.; Liu, Y.; Ling, C. D. Coexistence of ferroelectricity and magnetism in transition-metal doped n = 3 Aurivillius phases. *J. Phys.: Condens. Matter* **2008**, *20*, 025215.

(59) Wang, X.; Adhikari, J.; Smith, L. J. An Investigation of Distortions of the Dion-Jacobson Phase $RbSr_2Nb_3O_{10}$ and Its Acid-Exchanged Form with 93Nb Solid State NMR and DFT Calculations. *J. Phys. Chem. C* **2009**, *113*, 17548−17559.

(60) Rae, A. D.; Thompson, J. G.; Withers, R. L.; Willis, A. C. Structure refinement of commensurately modulated bismuth titanate $Bi_4Ti_3O_{12}$. *Acta Crystallogr., Sect. B: Struct. Sci.* **1990**, *B46*, 474−487.

(61) Benedek, N. A.; Mulder, A. T.; Fennie, C. J. Polar actahedral rotations: a path to new multifunctional materials. *J. Solid State Chem.* **2012**, *195*, 11−20.

(62) Hyatt, N. C.; Reaney, I. M.; Knight, K. S. Ferroelectric-paraelectric phase transition in the n = 2 Aurivillius phase $Bi_3Ti_{1.5}W_{0.5}O9$: a neutron powder diffraction study. *Phys. Rev. B: Condens. Matter Mater. Phys.* **2005**, *71*, 024119.

(63) Armstrong, A. R.; Anderson, P. A. Synthesis and structure of a new layered niobium blue bronze: $Rb_2LaNb_2O_7$. *Inorg. Chem.* **1994**, *33*, 4366−4369.